RSC Advances

ROYAL SOCIETY OF CHEMISTRY

www.rsc.org/advances

A table of contents entry

Color graphic

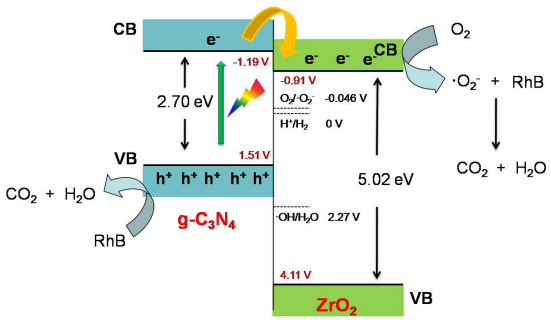

TEXT:

ZrO_2/g-C_3N_4 composite was prepared by directly heating ZrO_2-melamine mixture and showed excellent activity in rhodamine photodegradation.

Cite this: DOI: 10.1039/c0xx00000x

www.rsc.org/xxxxxx

ARTICLE TYPE

Synthesis and characterization of ZrO_2/g-C_3N_4 composite with enhanced visible-light photoactivity for rhodamine degradation

Xiaoxing Wang[a], Lihong Zhang [a], Hongjun Lin [c], Qinyan Nong[a], Ying Wu*[b], Tinghua Wu[b] and Yiming He*[a]

Received (in XXX, XXX) Xth XXXXXXXXX 20XX, Accepted Xth XXXXXXXXX 20XX
DOI: 10.1039/b000000x

The visible-light-driven ZrO_2/g-C_3N_4 hybrid photocatalysts were prepared by direct heating of ZrO_2 and melamine. Compared to pure g-C_3N_4 or ZrO_2, the synthesized ZrO_2/g-C_3N_4 exhibited much higher photocatalytic activity for rhodamine (RhB) degradation under visible light irradiation. In order to reveal the origin of the high photoactivity, the ZrO_2/g-C_3N_4 composites were characterized by various techniques including N_2 adsorption, thermogravimetric analysis (TG), X-ray diffraction (XRD), Fourier transform infrared spectroscopy (FT-IR), scanning electron microscopy (SEM), transmission electron microscopy (TEM), X-ray photoelectron spectroscopy (XPS), UV-vis diffuse reflectance spectroscopy (DRS), photoluminescence spectroscopy (PL), and electrochemical method. The characterization results demonstrated that ZrO_2 nanoparticles were well distributed on the surface of g-C_3N_4. Although the anchoring of ZrO_2 on g-C_3N_4 increased the surface area and light absorption ability, the formed hetero-junctions between the two semiconductors which retarded the recombination of electron and holes were believed to result in the enhanced photoactivity of ZrO_2/g-C_3N_4 composite. In addition, it was found that holes and $\bullet O_2^-$ generated in the photocatalytic process played a key role in RhB degradation over the ZrO_2/g-C_3N_4 hybrids.

1. Introduction

Since 1972, heterogeneous photocatalysis technique has received considerable attention as an attractive strategy in water purification and converting solar energy into the form of hydrogen by splitting water. A large number of metal oxide semiconductors, including TiO_2, ZnO and ZrO_2, have been investigated and reported [1-5]. However, their application in a large scale is greatly limited since they can only absorb the ultraviolet (UV) light which occupies no more than 4% of the solar spectrum. Therefore, several approaches, such as metal ions or non-metal ions doping, dye sensitization, and semiconductor doping, have been reported to extend their light response [6-11]. The last approach is considered as the most efficient way, and many semiconductors have been applied to improve their photocatalytic activity under visible light. An interesting phenomenon is that the modification is mainly focused on TiO_2 and ZnO [6-11], while few research concerned on ZrO_2 has been reported. The extra wide band gap might be the main reason, which induces the difficulty in shortening the band gap of ZrO_2. Another possible reason is its high conduction band. Based on the reported literature, the CB potential of ZrO_2 is estimated to be about -1.0 eV [12] which is more negative than that of TiO_2 (-0.12 eV) [3] and ZnO (-0.45 eV) [13]. Few semiconductors contain such negative CB that can be used to sensitize ZrO_2.

Recently, Wang and his coworkers reported a novel photocatalyst, graphitic carbon nitride (g-C_3N_4), which exhibits a high photocatalytic activity for the splitting of water into hydrogen using solar energy [14]. The metal-free semiconductor also exhibits activity for the degradation of organic pollutants and photocatalytic CO_2 reduction under visible light irradiation [15,16]. Combined with the merits of low cost, thermal and chemical stability, g-C_3N_4 semiconductor is considered as a valuable material for photocatalysis-driven applications. However, to date bare g-C_3N_4 still suffers the disadvantage of low quantum efficiency, which limits the photocatalytic performance. Therefore, a variety of semiconductors were decorated on g-C_3N_4 to improve its photoactivity [17-22]. For example, Wang et al. reported a Ag_3VO_4/g-C_3N_4 photocatayst and its application for triphenylmethane dye degradation [17]. The loading of Ag_3VO_4 greatly promoted the degradation rate of g-C_3N_4. Huang et al. synthesized CeO_2/g-C_3N_4 composite by mixing-calcination method and investigated its photoactivity in RhB photodegradation [18]. The results indicated that the photocatalytic activity of the composite material was enhanced by the loading of CeO_2. Other similar catalysts, such as $LnVO_4$ (Ln=Sm, La, Y, Bi)/g-C_3N_4 [19-22], WO_3/g-C_3N_4 [23], MoO_3/g-C_3N_4 [24], graphene/g-C_3N_4 [25], Ag_3PO_4/g-C_3N_4 [26], AgX/g-C_3N_4 [27], and CdS/g-C_3N_4 [28], were also reported. However, to the best of our knowledge, there has been no report regarding the coupling of g-C_3N_4 with ZrO_2 to enhance the photocatalytic activity. Actually, the conduction band (CB) of g-C_3N_4 is located at ~-1.2 eV [19], indicating g-C_3N_4 can sensitize ZrO_2. The ZrO_2 couped g-C_3N_4 composite might be an efficient photocatalyst.

In this study, we present the first example of a ZrO_2-

hybridized g-C_3N_4 photocatalyst fabricated by a mixing-calcination method. ZrO_2 is prepared by hydrothermal method and shows the morphology of nano spindle. After hybridization with the spindle-like ZrO_2, the visible photocatalytic activity of g-C_3N_4 for RhB photodegradation is effectively enhanced, demonstrating the hybrid effect existed between ZrO_2 and g-C_3N_4. On the basis of the investigation results, the origin of the hybrid effect is discussed.

2. Experimental Section

2.1 Catalysts preparation

All chemicals were analytical pure reagent and purchased commercially without further purification. Pure g-C_3N_4 was prepared by directly heating melamine at 520 ^oC in a muffle furnace for 4 h at a heating rate of 10 ^oC/min. The preparation of ZrO_2 referred to the previous literature [29]. Typically, 2.204 g cetyltrimethylammonium bromide (CTAB) was first dissolved in 40 mL water with stirring at 40 ^oC to obtain a clear micellar solution. Then 3.6 g zirconyl chloride was added to the solution. This combined solution was stirred for 15 min and then NaOH (1 mol/L) was added until the pH reached 11.5. After that, the mixture was transferred into a 100 mL autoclave with an inner Teflon lining and maintained at 100 ^oC for 24 h. The resulting white precipitate was collected by centrifugation, washed several times with ethanol and deionized water, and dried in an oven at 80 ^oC for 12 h.

The ZrO_2/g-C_3N_4 composites were prepared as follows: ZrO_2 and melamine with different ratio were mixed in a motor and then grounded for 30 min. The resultant mixed powder was put into a crucible with a cover and then heated at 520 ^oC in a muffle furnace for 4 h with a heating rate of 10 ^oC/min. After the temperature decreased to room temperature, the ZrO_2/g-C_3N_4 hybrids with various ZrO_2 contents were obtained. Thermogravimetric analysis (TG) was investigated to determine the weight contents of ZrO_2 in ZrO_2/g-C_3N_4. Based on the characterization results (Fig. S1), the ZrO_2/g-C_3N_4 composites with different ZrO_2 concentrations were named as 10wt.% ZrO_2/g-C_3N_4, 20.9wt.% ZrO_2/g-C_3N_4, 29.7wt.% ZrO_2/g-C_3N_4 and 36.1wt.% ZrO_2/g-C_3N_4, respectively.

2.2 Characterizations

The TG analysis (Netzsch STA449) of the catalysts was carried out in a flow of air (20 mL/min) at a heating rate of 10 ^oC/min. The N_2 adsorption measurement was performed on an Autosorb-1 (Quantachrome Instruments) by the Brunauer–Emmett–Teller (BET) method at 77 K. The XRD characterization of the catalysts was carried out on a Philips PW3040/60 using Cu Kα radiation. The SEM pictures were taken on a field emission scanning electron microscope (Hitachi S-4800). The TEM images were collected with a JEOL-2100F transmission electron microscope at an accelerating voltage of 200 kV. The DRS spectra of catalysts were recorded on a UV-vis spectrometer (Thermo Nicolet Evolution 500) using $BaSO_4$ as a reference sample. The XPS spectra were obtained by using a Quantum 2000 Scanning ESCA Microprobe instrument using AlKα. The PL spectra were collected on FLS-920 spectrometer (Edinburgh Instrument), using a Xe lamp (excitation at 365 nm) as light source.

The electrochemical impedance spectroscopy (EIS) and photocurrent responses (PR) measurements were performed using a CHI 660B electrochemical workstation with a standard three-electrode cell at room temperature. The prepared sample, Ag/AgCl (saturated KCl), and Pt wire were used as the working electrode, the reference electrode, and the counter electrode, respectively. The working electrodes was prepared as follows. An indium tin oxide (ITO) glass pieces with a size of 1.5×5 cm was cleaned successively by acetone, boiling NaOH (0.1 mol/L), deionized water, and dried in an air stream. Then, 0.018g sample and 0.002g polyvinylidene fluoride was mixed and ground for three minutes. After the addition of three drops of 1-Methyl-2-pyrrolidinone and the subsequently ultrosonic treatment for 20 min, the obtained suspension was coated onto the ITO glass substrate. The coated area on the ITO glass was controlled to be 0.8×0.8 cm. Finally, the coated ITO glass was dried at 50 ^oC to obtain the working electrode. The EIS spectra were recorded by applying an AC voltage of 10 mV amplitude in the frequency range of 10^5 Hz to 10^{-2} Hz with the initial potential (0 V) in 0.01 M Na_2SO_4. For PR measurement, a 350 W Xe arc lamp served as the light source and Na_2SO_4 (0.5 M) aqueous solution was used as the electrolyte.

2.3 Photocatalyic reaction

The photocatalytic activities of ZrO_2/g-C_3N_4 hybrids were tested by RhB (10 mg/L) degradation under visible-light irradiation in an apparatus. Visible light ($420 < \lambda < 800$ nm) generated by a 500 W Xe lamp equipped with two optical filters was used as the light source. The power density of visible light at the position of reactor was approximately 7.4 mW/cm^2 and the catalyst content was 0.2 g/100 mL. Prior to irradiation, the suspensions were magnetically stirred in dark for 60 min. During the RhB photodecomposition, samples were withdrawn at regular intervals and centrifuged to separate solid particles for analysis. The concentration of the RhB was determined by a UV–vis spectroscopy at its maximum absorption wavelength (about 554 nm). The examination experiment of reactive species is similar to the photodegradation experiment. A quantity of scavengers was introduced into the RhB solution prior to addition of the catalyst. The concentration of scavengers was controlled to be 0.01 mol/L according to the previous studies [30-33].

3. Results and discussion

3.1 Characterizations of ZrO_2/g-C_3N_4 composites.

The morphologies of pure g-C_3N_4, ZrO_2, and ZrO_2/g-C_3N_4 composite were investigated by SEM and TEM. ZrO_2 shows as spindle nanoparticles with an average particle size of 50 nm (Figures 1a and 1b), which leads to its high surface area of 43.2 m^2/g. Different from ZrO_2, pure g-C_3N_4 has a low surface area of 13 m^2/g, which can be attributed to its special morphology. As shown in Figures 2a and 2b, the polymer is shown as an aggregation of many sheets due to its layered structure [14]. The different morphologies of ZrO_2 and g-C_3N_4 make the two semiconductors be easily distinguished in the SEM image of ZrO_2/g-C_3N_4 composite. It can be observed that ZrO_2

nanoparticles are coated on the surface of g-C_3N_4 in the composite (Fig. 1e). The hybrid structure of ZrO_2/g-C_3N_4 composite can be verified further by the TEM analysis (Fig. 1f). ZrO_2 particles, which are darker than g-C_3N_4 due to its heavier atom, are observed to disperse finely on g-C_3N_4 sheets. In addition, considering that the ZrO_2/g-C_3N_4 was ultrasonicated for 30 min before the TEM analysis, the result in Fig. 1f indicates that ZrO_2 particles are closely adhered on g-C_3N_4 sheets and the interaction between ZrO_2 and g-C_3N_4 is strong, which is beneficial for the formation of ZrO_2-g-C_3N_4 hetero-junction. The BET surface areas result obtained via the method of N_2 adsorption shows that the addition of ZrO_2 increases the surface area of g-C_3N_4. The BET surface area of 10wt.% ZrO_2/g-C_3N_4, 20.9wt.% ZrO_2/g-C_3N_4, 29.7wt.% ZrO_2/g-C_3N_4 and 36.1wt.% ZrO_2/g-C_3N_4 samples are 21.7, 25.8, 33.1 and 36.4 m^2/g, respectively.

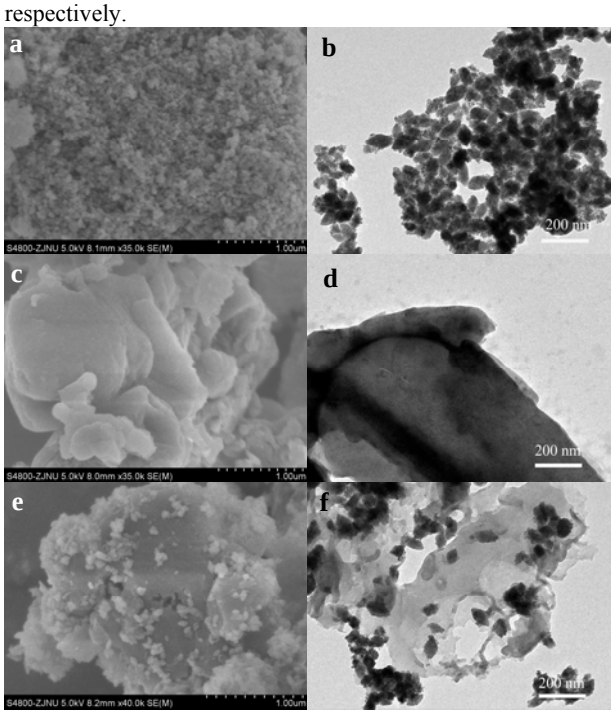

Fig. 1 SEM and TEM images of ZrO_2 (a,b), g-C_3N_4 (c,d), and 20.9wt.% ZrO_2/g-C_3N_4 composite (e,f).

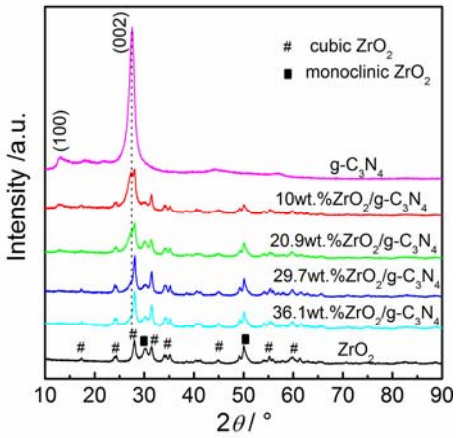

Fig. 2 XRD patterns of ZrO_2/g-C_3N_4 composites with different ZrO_2 concentration.

The crystalline structure of ZrO_2/g-C_3N_4 was investigated by XRD. The synthesized ZrO_2 consists of both monoclinic phase (JCPDS No. 37-1484) and body-centered cubic phase (JCPDS No. 49-1642). g-C_3N_4 shows its characterization peaks at 27.4 ° and 13.0 °, which can be indexed to (002) and (100) diffraction plane of the graphite-like carbon nitride [15]. For ZrO_2/g-C_3N_4 composite, it exhibits diffraction peaks corresponding to both g-C_3N_4 and ZrO_2. The diffraction peaks of ZrO_2 intensify gradually as the increase of ZrO_2 content, while the g-C_3N_4 peaks decrease. With the exception of ZrO_2 and g-C_3N_4, no other phase is detected, which reflects the hybrid structure of ZrO_2/g-C_3N_4.

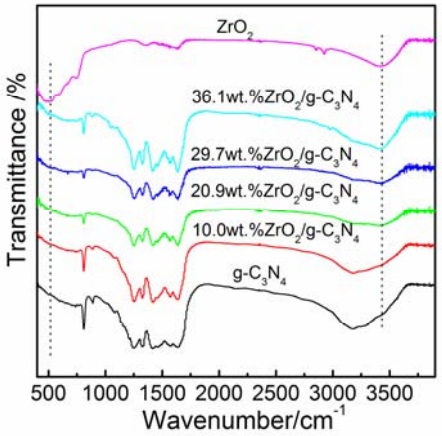

Fig. 3 FT-IR spectra of ZrO_2/g-C_3N_4 composites with different ZrO_2 concentration.

The FT-IR spectra of ZrO_2, g-C_3N_4, and ZrO_2/g-C_3N_4 composite are shown in Fig. 3. The broad absorption bands at around 509 cm^{-1} and 750 cm^{-1} are attributed to the Zr-O vibration absorption [34], while the broad absorption region with a maximum around 3446 cm^{-1} can be attributed to the hydroxyl groups of hydrated oxide surface and the adsorbed water [34]. For pure g-C_3N_4, the observed strong peaks in the range of 1200-1700 cm^{-1} can be ascribed to the typical stretching vibration of CN heterocycles [12]. The peak at 808 cm^{-1} can correspond to the breathing mode of triazine units [12]. In addition, a broad absorption band with a maximum around 3220 cm^{-1} corresponding to the N-H groups is also observed [12]. The FT-IR spectra of ZrO_2/g-C_3N_4 are similar with that of pure g-C_3N_4. However, the change in the bands of 509 and 3446 cm^{-1} with the variation of ZrO_2 content can still demonstrate the existence of ZrO_2 phase. The FT-IR result shows good coincidence with XRD analysis and indicates the hybrids structure production of ZrO_2/g-C_3N_4 composite.

Fig. 4 shows the XPS spectra of g-C_3N_4, ZrO_2, and ZrO_2/g-C_3N_4 composite. All the signals of C, N, Zr, O are detected in the survey XPS spectrum of ZrO_2/g-C_3N_4 composite (Fig. 4a), indicating its hybrids structure, which is consistent with the XRD and FT-IR experiments. The high-resolution C1s XPS spectrum of ZrO_2 shows one peak at 284.6 eV which can be attributed to the contaminated carbon [16,17]. In the case of g-C_3N_4 and ZrO_2/g-C_3N_4, another strong C1s peak is observed, which can be ascribed to the sp^2-bonded carbon (N–C=N) [16,17]. Meanwhile, the addition of ZrO_2 affects the binding energy (BE) of C1s of g-C_3N_4. The C1s BE of ZrO_2/g-C_3N_4 shifts from 287.7 eV to 287.4 eV,

indicating the interaction of ZrO_2 and g-C_3N_4, just as the previous literatures [35,36]. The same phenomenon is also observed in the Zr 3d XPS spectra. As shown in Fig. 4c, Zr $3d_{5/2}$ and $3d_{3/2}$ BE of ZrO_2 are located at 181.0 eV and 184.4 eV, respectively, which are very close to those reported in the literature for pure ZrO_2 [37]. As compared to pure ZrO_2, Zr 3d peak of ZrO_2/g-C_3N_4 exhibits a slight positive shift due to the interaction between ZrO_2 and g-C_3N_4. This kind of interaction is beneficial for the formation of hetero-junction between the two semiconductors and the subsequently promotion in separation of electron-hole pairs. Fig. 4d shows the valence band (VB) XPS spectra of g-C_3N_4 and ZrO_2. The position of the valence band edges of g-C_3N_4 and ZrO_2 are 1.51 eV and 4.11 eV, respectively.

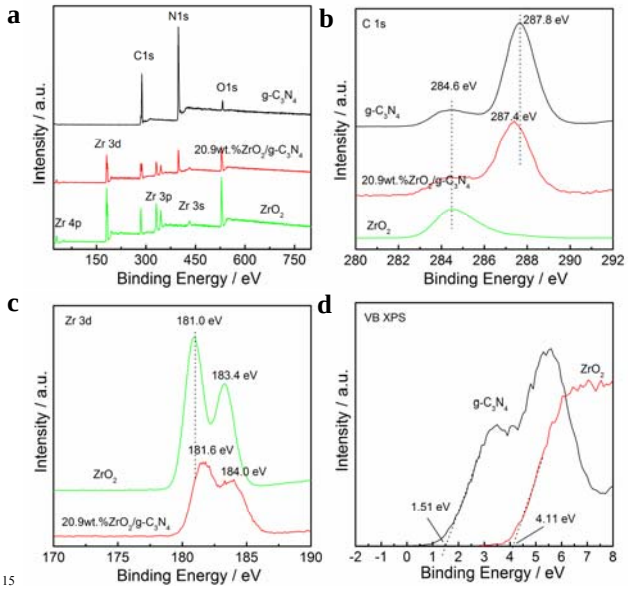

Fig. 4 XPS spectra of g-C_3N_4, ZrO_2, and 20.9wt.% ZrO_2/g-C_3N_4 composite. (a) survey spectra, (b) C1s, (c) Zr 3d, (d) VB XPS spectra of ZrO_2 and g-C_3N_4.

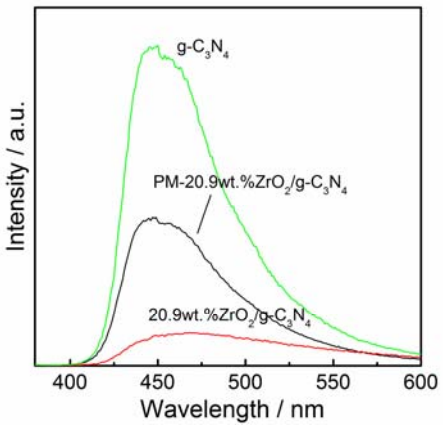

Fig. 5 PL spectra of 20.9wt.% ZrO_2/g-C_3N_4, PM-20.9wt.% ZrO_2/g-C_3N_4 and pure g-C_3N_4 excited at 365 nm.

The effect of the formed ZrO_2-g-C_3N_4 hetero-junction on the separation efficiency of electron-hole pairs was investigated by PL spectra. As shown in Fig. 5, a strong emission peak at around 460 nm is observed in pure g-C_3N_4, which can be attributed to the bandgap transition emission with the energy of emission light approximately equal to the bandgap energy of g-C_3N_4. However, in the PL spectrum of ZrO_2/g-C_3N_4, a considerable fluorescence quenching in the same position is detected, indicating that the addition of ZrO_2 significantly inhibits the recombination of electrons and holes [38]. For comparison, the PL spectrum of the physical mixture PM-20.9wt.%ZrO_2/g-C_3N_4 is also displayed in Fig. 5. The PL peak of PM-20.9wt.%ZrO_2/g-C_3N_4 is weaker than that of g-C_3N_4, but stronger than that of PM-20.9wt.%ZrO_2/g-C_3N_4, indicating that the decreased concentration of g-C_3N_4 contributes the weakened PL peak. However, there definitely exists charge transfer between g-C_3N_4 and ZrO_2 component, which further retards the recombination of electrons and holes.

In addition to the PL technique, EIS and transient photocurrent experiments are also effective methods to investigate the separation efficiency of electron-hole pairs in a photocatalyst. Fig. 6a shows the EIS changes of g-C_3N_4, ZrO_2, and 20.9wt.%ZrO_2/g-C_3N_4 electrodes. It can be observed that the arc size of the three electrodes is 20.9wt.%ZrO_2/g-C_3N_4 <ZrO_2<g-C_3N_4. In general, the decreased semicircle diameter indicates the smaller charge–transfer resistance on the electrode surface which results in an effective electron-hole separation [39-40]. Hence, the data in Fig. 6a suggests that ZrO_2/g-C_3N_4 composite has the highest efficiency in charge separation. The same result is also obtained by the transient photocurrent responses experiment. As shown from Fig. 6b, the photocurrent of 20.9 wt.% ZrO_2/g-C_3N_4 is much higher than that of g-C_3N_4 or ZrO_2, which proves the ZrO_2/g-C_3N_4 hybrid holds stronger ability in generating and transferring the photoexcited charge carrier under light irradiation [41,42].

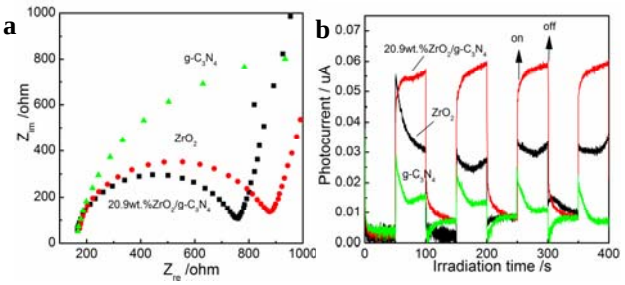

Fig.6 EIS changes (a) and transient photocurrent responses (b) of g-C_3N_4, ZrO_2, and 20.9wt.% ZrO_2/g-C_3N_4 electrodes.

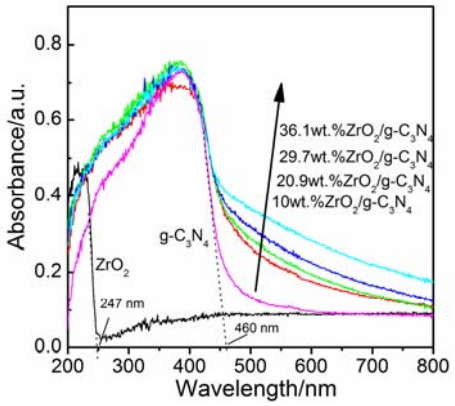

Fig. 7 UV-vis spectra of ZrO_2, g-C_3N_4 and ZrO_2/g-C_3N_4 composites.

The optical properties of g-C_3N_4, ZrO_2, and ZrO_2/g-C_3N_4 composites were measured via the UV-vis DRS technique. As shown in Fig. 7, white ZrO_2 can only absorb the light with a

wavelength shorter than 247 nm, and the band gap energy is about 5.02 eV. For pure g-C_3N_4, the absorbance edge locates at around 460 nm, and the band-gap energy is determined to be 2.7 eV which is in excellent agreement with the previous value [14,15]. The ZrO_2/g-C_3N_4 composite exhibits better photoabsorption performance than g-C_3N_4, which might be due to the interaction between ZrO_2 and g-C_3N_4. Some formed chemical bonds between the two semiconductors might result in the promoted optical property, similar as that in N-doped ZrO_2 [43] and graphene doped TiO_2 photocatalyst [44,45]. With increasing ZrO_2 content, the light absorption ability of ZrO_2/g-C_3N_4 is gradually strengthened. The results from DRS imply that the ZrO_2/g-C_3N_4 hybrids should possess visible-light photocatalytic activity.

3.2 Photocatalytic activities of ZrO_2/g-C_3N_4.

The degradation of RhB under visible light irradiation was carried out to evaluate the photocatalytic activity of as-prepared ZrO_2/g-C_3N_4 composites. Fig. 8a displays the changes of the RhB concentration versus the reaction time over ZrO_2/g-C_3N_4 photocatalysts with different ZrO_2 concentrations. The blank test shows that RhB is stable under visible light irradiation, which indicates that the contribution of RhB photolysis can be neglected. Pure ZrO_2 has a large surface area and exhibits good adsorption for RhB. Nearly half of RhB is adsorbed on ZrO_2 after one hour adsorption in the dark. Under visible light irradiation, some RhB are desorbed due to the increased temperature on the ZrO_2 surface, resulting in the enhanced RhB concentration at the beginning of the light-on. When the irradiation time is longer than 20 min, the concentration of RhB decreases slowly. This result indicates that a part of UV light may pass through the cutoff filter and induce the poor photoactivity of ZrO_2. Compared to ZrO_2, pure g-C_3N_4 has worse adsorption of RhB, but better photoactivity under visible light irradiation. The degradation rate is 0.012 min^{-1}, which is six times higher than that of ZrO_2. The decoration of ZrO_2 on g-C_3N_4 can promote the separation efficiency of electron-hole pairs and the light absorption ability, the catalytic activity for RhB degradation is thus enhanced. With the increase of ZrO_2 concentration from 10 wt.% to 31.6 wt.%, the photocatalytic activity of ZrO_2/g-C_3N_4 increases gradually and then decreases. 20.9wt.% ZrO_2/g-C_3N_4 sample exhibits the highest degradation rate of 0.028 min^{-1}, which is 2.33 times higher than that of g-C_3N_4.

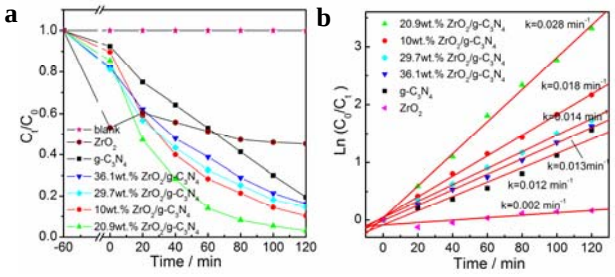

Fig. 8 Photodegradation of RhB over ZrO_2/g-C_3N_4 composites under visible light irradiation (a) and the corresponding reactive constant (b).

Although the high photoactivity of ZrO_2/g-C_3N_4 composite has been proven, the stability is important in view of its practical applications. Hence, the stability of the 20.9wt.% ZrO_2/g-C_3N_4 composite was investigated by a six-run cycling test under the same condition. For each run, the photocatalyst was recycled, cleaned, and dried. From Fig. 9a, the photodegradation efficiency of 20.9wt.% ZrO_2/g-C_3N_4 decreases slightly in the six cycles, which indicates that the ZrO_2/g-C_3N_4 photocatalysts can be reused completely for wastewater treatment. Fig. 9b shows the photocatalytic activity of 20.9wt.% ZrO_2/g-C_3N_4 with different scavenges. From Fig. 9b, it can be observed that 2-propanol (•OH quencher) [30,31] showed little effect on the reaction rate (k) of RhB degradation. However, the addition of benzoquinone (BQ, $•O^{2-}$ quencher) [32,33] leads to a great decrease of the k from 0.028 min^{-1} to 0.001 min^{-1}. The k also had an obvious drop to 0.05 min^{-1} in the presence of KI (h^+ and •OH quencher) [30,31]. This result indicates that h^+ and $•O^{2-}$ are two main reactive species in the photocatalytic process of ZrO_2/g-C_3N_4 hybrids.

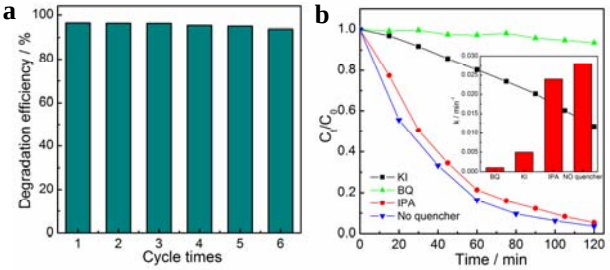

Fig. 9 The cycle test (a) and the reactive species trapping experiment (b) on 20.9wt.% ZrO_2/g-C_3N_4 composite.

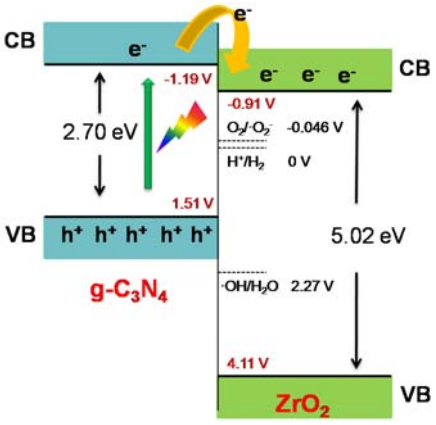

Fig. 10 Photocatalytic mechanism scheme of ZrO_2/g-C_3N_4 composite.

Therefore, it is clearly that the decoration of ZrO_2 on g-C_3N_4 generates an effective photocatalyst with high stability for the RhB degradation under visible light irradiation. The introduction of ZrO_2 can promote the surface area and light absorption capability of g-C_3N_4, which is beneficial for the photocatalytic reaction. However, the data in Fig. 8a shows that the photocatalytic activity of ZrO_2/g-C_3N_4 does not always increase with the enhancement of the two characters. For example, 36.1wt.% ZrO_2/g-C_3N_4 exhibits the highest surface area and light absorption ability. However, its photoactivity is much lower than that of 20.9wt.% ZrO_2/g-C_3N_4. This result indicates that the surface area and light absorption ability are not the dominant factor in affecting the photocatalytic activity of ZrO_2/g-C_3N_4. The key factor is the separation efficiency of electron-hole pairs. The

VB edges of ZrO_2 and g-C_3N_4 have been determined to be 4.11 eV and 1.51 eV via the VBXPS experiment, respectively. The CB edge potentials of the two semiconductors are thus obtained by using the equation of $E_{CB}=E_{VB}-E_g$. As shown in Fig. 10, the CB potential of g-C_3N_4 is -1.19 eV, which is more negative than that of ZrO_2. Under visible light irradiation, the electrons are excited from VB to CB in g-C_3N_4, which generates holes in VB of the semiconductor. The photogenerated electrons on g-C_3N_4 surfaces can easily transfer to ZrO_2 due to the difference in CB edge potentials, whereas the holes stay on the VB of g-C_3N_4. This process can effectively improve the separation of photogenerated electron-hole pairs and greatly decrease the possibility of charge recombination, resulting in the high photoactivity of ZrO_2/g-C_3N_4 composites, as proven in the PL, EIS, photocurrent and photocatalytic tests. Meanwhile, based on the mechanism in Fig. 10, the interface between ZrO_2 and g-C_3N_4 is important for the charge transfer and separation of electron-hole pairs. Excess ZrO_2 would aggregate on the g-C_3N_4 surface, which reduces the interface area between ZrO_2 and g-C_3N_4 and thereby lowers the charge separation efficiency. That's why there exists an optimal concentration of ZrO_2. The photogenerated electrons and holes are the origin of the photocatalytic reaction. Because the CB edge potential of ZrO_2 is more negative than $E_{O2/\bullet O2-}$ (-0.046 V) [46], the electrons in ZrO_2 can capture O_2 and reduce it to $\bullet O_2^-$ which has been proven to be one of the main reactive species. For the holes in g-C_3N_4, the reaction of h^+ with H_2O to generate •OH cannot occur due to the high VB position [1,31]. Instead, the holes directly oxidize the adsorbed RhB to inorganic products. The possible mechanism may be described as follows:

$$ZrO_2/g\text{-}C_3N_4 \xrightarrow{hv} ZrO_2/g\text{-}C_3N_4(e^- + h^+) \quad (1)$$

$$ZrO_2/g\text{-}C_3N_4(e^- + h^+) \longrightarrow ZrO_2(e^-)/g\text{-}C_3N_4(h^+) \quad (2)$$

$$O_2 + e^- \rightarrow \bullet O_2^- \quad (3)$$

$$\bullet O_2^- / h^+ + \text{RhB} \rightarrow \text{degradation pruducts} \quad (4)$$

4. Conclusion

In this work, an enhanced visible-light-driven photocatalyst of ZrO_2/g-C_3N_4 was prepared by directly calcination of ZrO_2 and melamine. Among the prepared hybrid photocatalysts, the 20.9 wt.% ZrO_2/g-C_3N_4 sample exhibited the optimal photocatalytic activity for RhB degradation under visible-light irradiation. The synergetic effect between ZrO_2 and g-C_3N_4 which resulted in efficient separation of electron-hole pairs was believed to be the origin of the high photocatalytic activity. Furthermore, the reusability experiments suggested that the photocatalytic material possessed good stability. This work might provide a promising approach for treatment of dye wastewater.

Acknowledgements

We acknowledge Dr. Xiaodong Yi in Xiamen University for his help in XPS analysis. This work was financially supported financially supported by Natural Science Foundation of Zhejiang Province in China (LY14B030002), the National Natural Science Foundation of China (51108424) and the Open Research Fund of Top Key Discipline of Chemistry in Zhejiang Provincial Colleges and Key Laboratory of the Ministry of Education for Advanced Catalysis Materials (Zhejiang Normal University).

[a] *Department of Materials Physics, Zhejiang Normal University, Jinhua, 321004, China. Fax: +86-0579-83714946; Tel: +86-0579-83792294; E-mail: hym@zjnu.cn*

[b] *Institute of Physical Chemistry, Zhejiang Normal University, Jinhua, 321004, China. Fax: +86-0579-83714946; Tel: +86-0579-83792294; E-mail: ying-wu@zjnu.cn*

[c] *College of Geography and Environmental Sciences, Zhejiang Normal University, Jinhua, 321004, China*

† Electronic Supplementary Information (ESI) available: TG profiles of pure g-C_3N_4 and ZrO_2/g-C_3N_4 composites (Fig. S1). See DOI: 10.1039/b000000x/

Notes and references

1. A. Fujishima, T.N. Rao, D.A. Tryk, *J. Photochem. Photobiol. C: Photochem. Rev.* 2000, **1**, 1–21.
2. X.B. Chen, S.H. Shen, L.J. Guo, S.S. Mao, *Chem. Rev.*, 2010, **110**, 6503–6570.
3. K. Mori, H, Yamashita, M. Anpo, *RSC Adv.*, 2012, **2**, 3165–3172.
4. A. Mclaren, T. Valdes-Solis, G.Q. Li, S.C. Tsang, *J. Am. Chem. Soc.*, 2009, 131, 12540–12541.
5. Y. Kohno, T. Tanaka, T. Funabiki, S. Yoshida, *Chem. Commun.*, 1997, 841–842.
6. W. Choi, A. Termin, M.R. Hoffmann, *J. Phys. Chem.*, 1994, **98**, 13669–13679.
7. R. Ashi, T. Morikawa, T. Ohwaki, K. Aoki, Y. Taga, *Science*, 2001, **293**, 269–271.
8. G.H. Qin, Z. Sun, Q.P. Wu, L. Lin, M. Liang, S. Xue, *J. Hazard. Mater.*, 2011, **192**, 599–604.
9. X.C. Wang, J.C. Yu, Y.L. Chen, L. Wu, X.Z. Fu, *Environ. Sci. Technol.*, 2006, **40**, 2369–2374.
10. X. Yang, J. Qin, Y. Li, R. Zhang, H. Tang, *J. Hazard. Mater.*, 2013, **261**, 342–350.
11. X. Yang, J. Qin, Y. Jiang, R. Li, Y. Li, H. Tang, *RSC Adv.*, 2014, **4**, 18627–18636.
12. K. Sayama, H. Arakawa, *J. Phys. Chem.*, 1993, **97**, 531–533.
13. A. Kushwaha, M. Aslam, *Electrochim. Acta*, 2014, **130**, 222–231.
14. X.C. Wang, K. Maeda, A. Thomas, K. Takanabe, G. Xin, J.M. Carlsson, K. Domen, M. Antonietti, *Nat. Mater.*, 2009, **8**, 76–80.
15. S.C. Yan, Z.S. Li, Z.G. Zou, *Langmuir*, 2009, **25**, 10397–10401.
16. J. Mao, T.Y. Peng, X.H. Zhang, K. Li, L.Q. Ye, L. Zan, *Catal. Sci. Technol.*, 2013, **3**, 1253–1260.
17. S.M. Wang, D.L. Li, C. Sun, S.G. Yang, Y. Guan, H. He, *Appl. Catal. B: Environ.*, 2014, **144**, 885–892.
18. L.Y. Huang, Y.P. Li, H. Xu, Y.G. Xu, J.X. Xia, K. Wang, H.M. Li, X.N. Cheng, *RSC. Adv.*, 2013, **3**, 22269–22279.
19. T.T. Li, L.H. Zhao, Y.M. He, J. Cai, M.F. Luo, J.J. Lin, *Appl. Catal. B: Environ.*, 2013, **129**: 255–263.
20. Y.M. He, J. Cai, L.H. Zhang, X.X. Wang, H.J. Lin, B.T. Teng, L.H.

Zhao, W.Z. Weng, H.L. Wan, M.H. Fan, *Ind. Eng. Chem. Res.*, 2014, **53**, 5905–5915.
21. J. Cai, Y.M. He**,** X.X. Wang, L.H. Zhang, L.Z. Dong, H.J. Lin, L.H. Zhao, X.D. Yi, W.Z. Weng, H.L. Wan, *RSC Adv*, 2013, **3,** 20862–20868.
22. Y.X. Ji, J.F. Cao, L.Q. Jiang, Y.H. Zhang, Z.G. Yi, *J. Alloy Compd.*, 2014, **590**, 9–14.
23. Y.P. Zang, L.P. Li, Y. Zuo, H.F. Lin, G.S. Li, X.F. Guan, *RSC Adv.*, 2013, **3**, 13646–13650.
24. Y.M. He, L.H. Zhang, X.X. Wang, Y. Wu, H.J. Lin, L.H. Zhao, W.Z. Weng, H.L. Wan, M.H. Fan, *RSC Adv.*, 2014, **4**, 13610–13619.
25. G.Z. Liao, S. Chen, X. Quan, H.T. Yu, H.M. Zhao, *J. Mater. C*hem., 2012, **22**, 2721–2726.
26. P.Z. He, L.M. Song, S.J. Zhang, X.Q. Wu, Q.W. Wei, *Mater. Res. Bull.,* 2014, **51**, 432–437.
27. H. Xu, J. Yan, Y.G. Xu, Y.H. Song, H.M. Li, J.X. Xia, C.J. Huang, H.L. Wan, Appl. Catal. B: Environ., 2013, **129**, 182–193.
28. J.Y. Zhang, Y.H. Wang, J. Jin, J. Zhang, Z. Lin, F. Huang, J.G. Yu, *ACS Appl. Mater. Interf.,* 2013, **5**, 10317−1032.
29. P. Trens, M.J. Hudson, R. Denoyel, *J. Mater. Chem.,* 1998, **8**, 2147–2152.
30. G.T. Li, K.H. Wong, X.W. Zhang, C. Hu, J.C. Yu, R.C.Y. Chan, P.K. Wong, *Chemosphere*, 2009, **76**, 1185–1191.
31. Y.M. He, J. Cai, T.T. Li, Y. Wu, H.J. Lin, L.H. Zhao, M.F. Luo, *Chem. Eng. J.*, 2013, **215-216**, 721–730.
32. X. Yang, H. Cui, Y. Li, J. Qin, R. Zhang, H. Tang, *ACS Catal.,* 2013, **3**, 363–369.
33. H. Cui, X. Yang, Q. Gao, H. Liu, Y. Li, H. Tang, X. Yan, *Mater. Lett.,* 2013, **93**, 28–31.
34. Q. Zhang, Y. Zhang, H.T. Li, C.G. Gao, Y.X. Zhao, *Appl. Catal. A: Gen.*, 2013, **466**, 233–239.
35. C.S. Pan, J. Xu, Y.J. Wang, D. Li, Y.F. Zhu, *Adv. Fun. Mater.*, 2012, **22**, 1518–1524.
36. X.X. Wang, S.S. Wang, W.D. Hu, J. Cai, L.H. Zhang, L.Z. Dong, L.H. Zhao, Y.M. He, *Mater. Lett.,* 2014, **115**, 53–56.
37. S. Velu, K. Suzuki, C.S. Gopinath, H. Yoshida, T. Hattori, *Phys. Chem. Chem. Phys.*, 2002, **4**, 1990–1999.
38. L.Q. Jing, Y.C. Qu, B.Q. Wang, S.D. Li, B.J. Jiang, L.B. Yang, W. Fu, H.G. Fu, J.Z. Sun, *Sol. Energ. Mat. Sol. C.*, 2006, **90**, 1773–1787.
39. H.T. Yu, X. Quan, S. Chen, H.M. Zhao, Y.B. Zhang, *J. Photochem. Photobiol. A: Chem.*, 2008, **200**, 301–306.
40. J. Lim, D. Monllor-Satocaa, J.S. Jang, S. Lee, W. Choi, *Appl. Catal. B: Environ.,* 2014, **152–153**, 233–240.
41. L.Z. Dong, Y.M. He, T.T. Li, J. Cai, W.D. Hu, S.S. Wang, H.J. Lin, M.F. Luo, X.D. Yi, L.H. Zhao, W.Z. Weng, H.L. Wan, *Appl. Catal. A: Gen.,* 2014**, 472**, 143–151.
42. Y.P. Bi, S.X. Ouyang, J.Y. Cao, J.H. Ye, *Phys. Chem. Chem. Phys.,* 2011, **13**, 10071–10075.
43. Y.Y. Zhao, Y.C. Zhang, J. Li, X.H. Du, *Mater. Lett.,* 2014, **13**0, 139–142.
44. K. Woan, G. Pyrgiotakis, W. Sigmund, *Adv. Mater.,* 2009, **21**, 2233–2239.
45. R. Leary, A. Westwood, *Carbon*, 2011, **49**, 741–772.
46. D.F. Wang, T. Kako, J.H. Ye, *J. Am. Chem. Soc.,* 2008, **130**, 2724–2725.